MITSUBISHI ELECTRIC RESEARCH LABORATORIES
http://www.merl.com

Urban Peer-to-Peer MIMO Channel Measurements and Analysis at 300 MHz

Gunnar Eriksson, Sara Linder, Kia Wiklundh, Peter Holm, Peter Johansson, Fredrik Tufvesson, Andreas Molisch

TR2008-076 December 2008

Abstract

Multiple-input multiple-output (MIMO)systems operating at frequencies in the upper VHF and lower UHF region is attractive for peer-to-peer communication applications where robustness is of high importance, e.g., in tactile networks and emergency response systems. When designing and evaluating such systems, knowledge of realistic propagation conditions is required. This paper presents results from an uran MIMO measurement campaign at 300 MHz. Measurements are performed along 25 receiver routes and for three fixed transmitter locations, using antenna arrays mounted on two cars. Channel characteristics and ergodic capacity for the 7X7 MIMO channels are extracted from the measured data. A path-loss model is derived for the measured scenario, and the distributions of the large-scale fading, the Ricean K-factor, the delay spread, and the ergodic capacity are studied in deatail. The correlation distance for the different channel parameters is also examined. Furthermore, the analysis reveals that several of the channel parameters are correlated, and also have a strong correlation with the capacity.

MILCOM 2008

Urban Peer-to-Peer MIMO Channel Measurements and Analysis at 300 MHz

Gunnar Eriksson*†, Sara Linder*, Kia Wiklundh*, Peter D. Holm*,
Peter Johansson*, Fredrik Tufvesson† and Andreas F. Molisch†‡

*FOI, Swedish Defence Research Agency, Box 1165, SE-581 11 Linkoping, Sweden
Email: {gunnar.eriksson, sara.linder, kia.wiklundh, peter.holm, petjoh}@foi.se
†Dept. of Electrical and Information Technology, Lund University, SE-221 00 Lund, Sweden
Email: {fredrik.tufvesson, andreas.molisch}@eit.lth.se
‡Mitsubishi Electric Research Labs, 201, Broadway, Cambridge, MA 02139, USA

***Abstract*—Multiple-input multiple-output (MIMO) systems operating at frequencies in the upper VHF and lower UHF region is attractive for peer-to-peer communication applications where robustness is of high importance, e.g., in tactical networks and emergency response systems. When designing and evaluating such systems, knowledge of realistic propagation conditions is required. This paper presents results from an urban MIMO measurement campaign at 300 MHz. Measurements are performed along 25 receiver routes and for three fixed transmitter locations, using antenna arrays mounted on two cars. Channel characteristics and ergodic capacity for the 7×7 MIMO channels are extracted from the measured data. A path-loss model is derived for the measured scenario, and the distributions of the large-scale fading, the Ricean K-factor, the delay spread, and the ergodic capacity are studied in detail. The correlation distance for the different channel parameters is also examined. Furthermore, the analysis reveals that several of the channel parameters are correlated, and also have a strong correlation with the capacity.**

I. Introduction

For mission success it is essential to achieve information awareness. The services needed in a mobile tactical wireless network to achieve this have high demands on communication capacity and reliability. This must also be achieved in a variety of environments, including urban areas. Peer-to-peer communications are important for such networks, as well as for many other applications, like emergency response systems. From a wave propagation point of view, the peer-to-peer communication scenario is more challenging than scenarios with elevated base stations, e.g., cellular communication systems. Due to the low height of both the transmitter (Tx) and receiver (Rx), line-of-sight (LOS) conditions rarely exists. The robustness of wireless communication systems is strongly related to the frequency they operate on. Frequencies in the upper VHF and lower UHF regions are very attractive for mobile tactical networks. Due to the large wavelength, the waves can more easily diffract around obstacles compared to the case at higher frequencies [1]. Furthermore, the frequency is high enough to allow terminals with multiple antenna elements, at least for vehicular terminals. The absolute bandwidth available for a communication system in this frequency range is, however, quite limited. Thus, to meet the demands for high data rates, spectral efficiency is very important and multiple-input multiple-output (MIMO) communication systems is a very promising way to achieve this. In fading environments MIMO systems have shown to offer a large capacity increase over single-input single-output (SISO) systems [2]–[4]. In theory the capacity increases linearly with the minimum of the number of Tx and Rx antennas. However, in real environments, the achievable capacity depends on the radio-channel characteristics.

In order to design and evaluate MIMO systems for tactical communication networks, relevant and realistic channel models are required. However, no suitable peer-to-peer MIMO channel models exist for for frequencies around 300 MHz. Most of the MIMO channel measurements and proposed models in the literature are for significantly higher frequencies (mostly 2 and 5 GHz), typically for cellular and personal wireless communication systems. In [5], an overview of such work is given. Measurements of angular properties is analyzed for a peer-to-peer scenario at 1.9 GHz in [6]. Analysis of achievable capacities and wideband characteristics for peer-to-peer MIMO scenarios at 2.5 GHz are presented in [7] and [8]. For SISO systems, measurements and analysis have been conducted for lower frequencies. For example, narrowband measurements have been performed at 400 MHz for design and evaluation of the TETRA system [9], see e.g. [10]. Path loss investigations in an urban environment for tactical systems at 225, 450 and 900 MHz are presented in [11]. Furthermore, [12] reports wideband measurements at 400 MHz, and [13] demonstrated the feasibility of wideband, spectrally efficient MIMO peer-to-peer communications at 456, 904, and 2177 MHz. Moreover, double-directional channel measurements at 300 MHz, in a semi-rural and suburban environment, is presented in [14].

In this work we present results from a peer-to-peer MIMO measurement campaign at 300 MHz in an urban environment. We focus on basic channel characteristics, which are important for the development and validation of realistic channel models. Specifically, we investigate the distance dependency of the path gain, the distributions for the large-scale fading, the Ricean K-factor, delay spread, and the ergodic capacity

978-1-4244-2677-5/08/$25.00

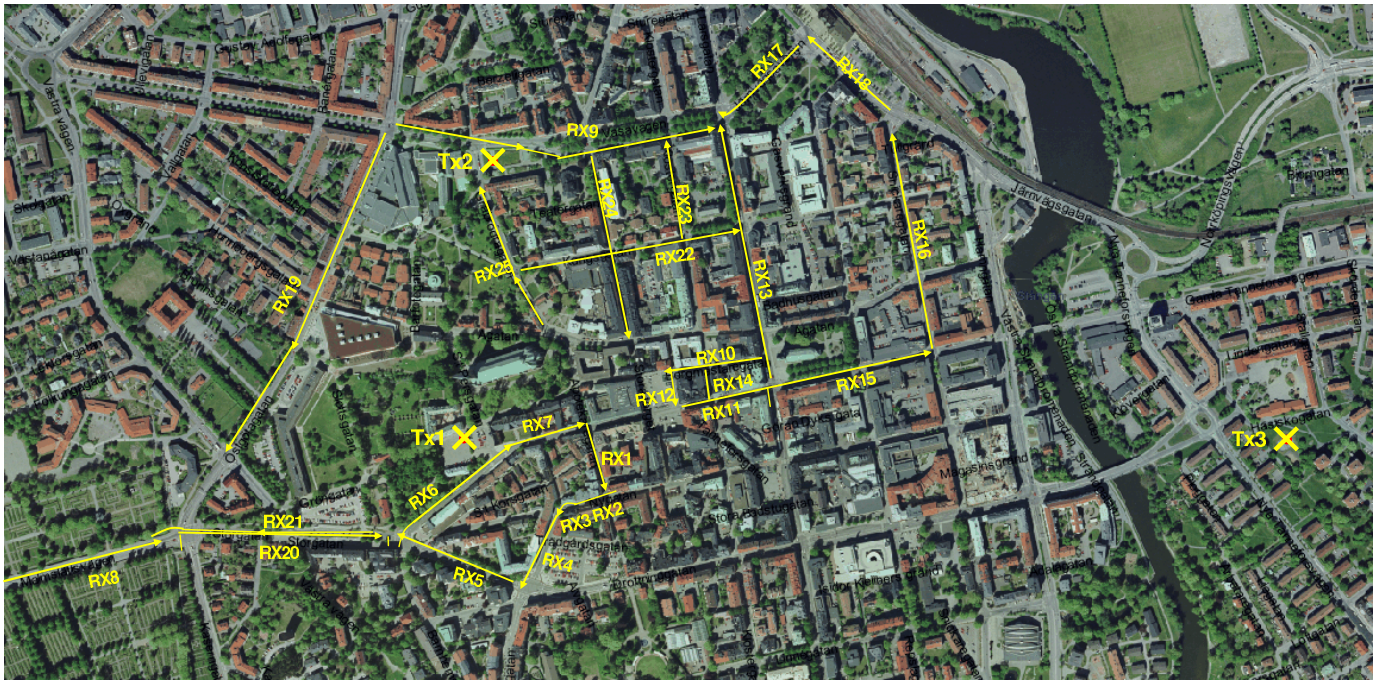

Fig. 1. Measurement area in the city center of Linkoping, Sweden. Transmitter sites (crosses) and receiver routes (arrows).

(evaluated at a fixed signal-to-noise ratio (SNR)). Furthermore, the difference between the local (per measured route) distributions and the global distributions (for the scenario) is studied. In addition, the correlation distance of the parameters is examined. Moreover, we analyze the correlation between the channel parameters, as well as the correlation between capacity and the channel parameters.

The remainder of the paper is organized as follows: Sec. II describes the measurement equipment and the environment for the urban MIMO measurement campaign. In Sec. III, the results from our analyses are presented, and finally, in Sec. IV summary and conclusions are given.

II. Measurement Equipment and Scenario

Measurement data were collected with the RUSK-LUND MIMO channel sounder, which sequentially measures the channel between all combinations of transmit and receive antenna elements within a short time interval. (For a description of the measurement principle, see [15], [16].) The measurements were performed at a center frequency of 285 MHz and the 20 MHz wide probing signal was a 12.8 μs long, periodically repeated sequence, hence giving a spectrum of 257 frequency lines with a separation of 78.125 kHz. Since the antenna element switching takes place every second period of the probing sequence, delays up to 12.8 μs could be measured unambiguously; which was more than sufficient in this environment. One full switching cycle, which takes about 1.8 ms, constitutes a channel snapshot. The channel transfer function was obtained by comparing each frequency line in the measured data with the corresponding frequency lines in the data recorded during system calibration. The output power was 43 dBm and a vertically polarized antenna array was used at both the Tx and Rx. Each array is a seven element uniform circular dipole array (UCDA) with a radius of 0.6 m. One additional center element is located in an elevated position with respect to the UCDA. Furthermore, a cylindrical reflector is placed in the center of the UCDA giving each of the 7 elements a directional radiation pattern. The Tx and the Rx were both placed in cars with the antenna arrays mounted on top of each car. The antenna heights were approximately 1.8 and 2.1 meters above the ground for the Tx and Rx, respectively. A wheel sensor on the Rx vehicle controlled the data recording by giving a trigger pulse every 0.24 m. At each pulse, a data block of 4 channel snapshots was recorded. These 4 snapshots were in the following data processing coherently averaged to increase the SNR. Hence, the measurement output for data block i, is a channel transfer matrix estimate $\mathbf{H}_i$ of size $n_{\text{rx}} \times n_{\text{tx}}$, where n_{rx} and n_{tx} are the number of Rx and Tx elements, respectively. Each element of $\mathbf{H}$ contains the frequency channel transfer function at the measured 257 spectral lines.

The measurement campaign was conducted in the city center of Linkoping, which is the 5th largest city in Sweden, but by international standards a rather small town with about 100,000 inhabitants. Fig. 1 shows an aerial photo of the measurement area. This part of the town, which typically has three- to six-story buildings, is rather flat but slopes gently towards the river on the east side. The measured scenario consists of 3 different Tx locations and 25 Rx routes. The length of the routes varies considerably as their start and stop positions were chosen to obtain as straight lines as possible, with easily identifiable references in the environment. During the measurements the Tx was stationary at each site, while

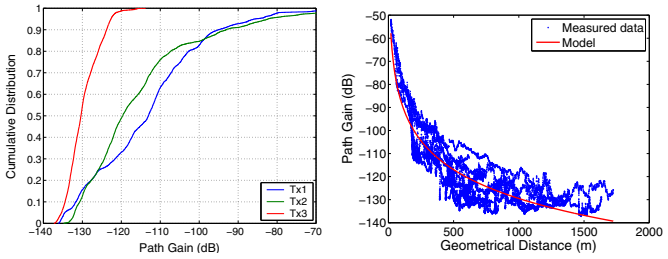

(a) (b)

Fig. 2. Measured path gain G_{meas}. (a) CDFs for the 3 Tx sites. (b) All measurements vs. geometrical distance; the fitted model $G_{\text{d}}(d)$ shown as a red solid line.

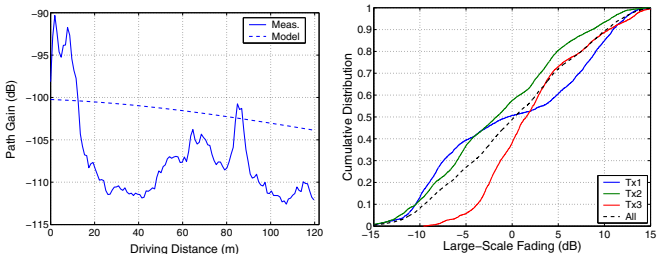

(a) (b)

Fig. 3. (a) Measured path gain G_{meas} and modeled path gain G_{d} along Route 1 for Tx1. (b) CDF for the large-scale fading from each Tx.

the Rx was driven along the measurement routes. The three Tx sites are in the following referred to as Tx1, Tx2, and Tx3, respectively. Tx1 is located in a small square, with a few buildings 20–50 m away, and with a park with very dense vegetation of high trees on the west side. Tx2 is in the west end of a small park. There are buildings about 35 m to the south and to the west, and about 50 m to the north of Tx2. Finally, Tx3 is located in a small and open park east of the river. The closest buildings are about 40 m to the north of Tx3. More buildings are located about 70 m to the south-east.

A few Tx–Route combinations were not measured due to time constraints. For Tx1, Route 22–25 are missing; and for Tx3, Route 20 is missing.

III. Results

A. Path-Gain Model

The path gain (reciprocal of path loss) $G = P_R/P_T$, with P_R and P_T denoting the received and transmitted power, respectively, was calculated for every measured data block by averaging the received power over all frequency subchannels, and over all combinations of transmit and receive antenna elements. Due to the large diversity order therby achieved, no significant fast fading could be observed. Finally, the path gain was averaged over 4 consecutive data blocks, thus providing a result G_{meas} for every 0.96 m along the route. The cumulative distribution function (CDF) for G_{meas} is presented in Fig. 2(a) for the three Tx locations. The CDFs show that the path gain for Tx3 in general is significantly smaller than for Tx1 and Tx2. This is expected since the geometrical distances (see, Fig. 1) for Tx3 are generally larger than for the other two sites. In Fig. 2(b), the measured path gain G_{meas} for all routes and Tx combinations is shown as a scatter plot vs. the geometrical distance.

The distance-dependent part of the path gain is modeled to be a function of the geometrical distance, d, as

$$G_{\text{d}}(d) = G_0 - 10n\log_{10}\left(\frac{d}{d_{\text{ref}}}\right), \quad [\text{dB}] \tag{1}$$

where G_0 is the path gain at the reference distance d_{ref} and n is the path gain exponent. The two parameters G_0 and n was estimated by regression analysis of G_{meas} (expressed in dB). To maintain a dataset that spans a reasonable large interval of geometrical distances, it was not considered feasible to estimate model parameters per route, as the range of distances for many of the routes (especially those almost orthogonal to the LOS path) is very limited. Thus, all data (all Tx–Route combinations) were combined, except that Route 8 was excluded for Tx position 3. The reason is that this Tx–Route combination is the only one with a geometrical distance exceeding 2 km, and hence might have a disproportionate influence on the resulting model parameters. From the regression analysis, the values of the parameters are found to be $n = 4.15$ and $G_0 = -4.84$ dB for a reference distance, d_{ref}, of 1 m. The resulting model $G_{\text{d}}(d)$ is depicted by the solid red line in Fig. 2(b).

B. Large-Scale Fading

The large-scale fading, i.e., the variations in the path gain that are not attributed to variations in the geometrical distance, is computed as

$$G_{\text{LS}}(r) = G_{\text{meas}}(r) - G_d\big(d(r)\big), \quad [\text{dB}] \tag{2}$$

where $G_{\text{d}}(d(r))$ is obtained from the model (1), r is the driving distance (position) along the route, and $d(r)$ is the geometrical distance between Tx and Rx. As an example, Fig. 3(a) shows $G_{\text{meas}}(r)$ and $G_d(d(r))$ along Route 1 for Tx1. Here, the large-scale fading is positive for the first 10 m, but negative for the rest of the route; except at the peak at 85 m. From the distribution for $G_{\text{LS}}(r)$ for all routes, shown in Fig. 3(b), we see that the variation around the distance-dependent model is about ± 15 dB in this scenario, with a standard deviation of 7.2 dB for all Tx positions together. A closer examination of the geometrical distance dependency of the path gain, where each Tx–Route combination could be identified, reveals that most Tx–Route pairs have an offset relative to $G(d(r))$, and that this offset is more or less maintained along each route. This behavior is investigated by computing $\bar{G}_{\text{LS}}$ and $\bar{\sigma}_{G_{\text{LS}}}$, the per route and Tx position mean and standard deviation of $G_{\text{LS}}(r)$. The CDFs for this "local" statistics are given in Fig. 4 for each Tx position separately and for all Tx positions combined. The CDFs show that $\bar{G}_{\text{LS}}$ varies about ± 12 dB for the different routes, and that $\bar{\sigma}_{G_{\text{LS}}}$ has a median value of 2.4 dB. The distribution for Tx3 differs from the other two by not having any mean values less than -6.2 dB. Tx3 has

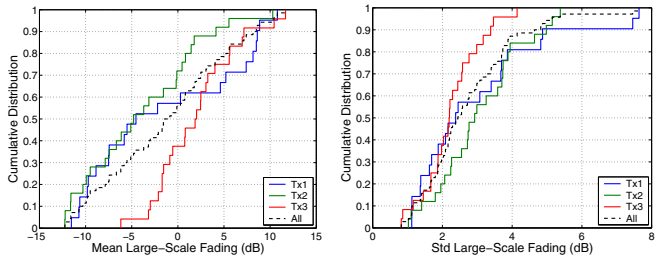

(a) (b)

Fig. 4. Large-scale fading per-route statistics. (a) Mean. (b) Std.

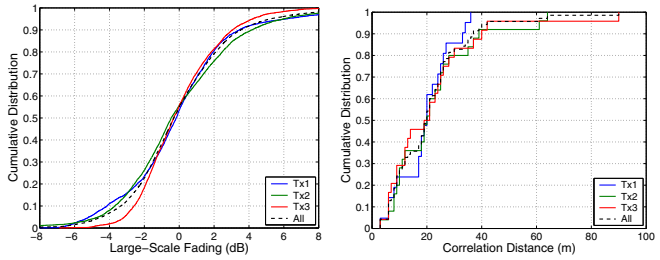

(a) (b)

Fig. 5. (a) CDF for large-scale fading zero-mean process $\widetilde{G}_{\rm LS}(r)$. (b) CDF for the large-scale fading correlation distance.

a large numbers of long geometrical distances and for these distances the model (1) gives a larger loss than the majority of the measurements. Considering all transmitters, the observed distribution for $\bar{G}_{\rm LS}$ is (in dB scale) close to uniform.

From the observations above, it can be assumed that the zero-mean fading process

$$\widetilde{G}_{\rm LS}(r) = G_{\rm LS}(r) - \bar{G}_{\rm LS}, \tag{3}$$

obtained by removing $\bar{G}_{\rm LS}$ from the large-scale fading variations for each route and Tx combination, would be more stationary and vary less than $G_{\rm LS}(r)$. The CDF for $\widetilde{G}_{\rm LS}(r)$ is shown in Fig. 5(a) for each Tx position, as well as for the Tx positions combined. The distributions are very similar, except for that the distribution for Tx3 is slightly narrower. The standard deviations are 3.40, 3.36, 2.32, and 3.09 for Tx1, Tx2, Tx3, and all Tx, respectively. Comparing these distributions with those for $G_{\rm LS}$ in Fig. 3(b), it is clear that the large-scale fading within the "local" per-route environments are significantly less than what is obtained for the global scenario.

The correlation distance of $G_{\rm LS}(r)$ is an important statistical property of the large-scale fading process. The large-scale fading autocovariance function is

$$R_{G_{\rm LS}}(\Delta r) = E\Big\{\widetilde{G}_{\rm LS}(r)\,\widetilde{G}_{\rm LS}(r+\Delta r)\Big\}, \tag{4}$$

where Δr is the separation distance along the route, and $E\{\cdot\}$ denotes the expectation operator. We define the correlation distance as the smallest (non-negative) Δr for which $\rho_r(\Delta r) \leq 0.5$, where $\rho_r(\Delta r) = R_{G_{\rm LS}}(\Delta r)/R_{G_{\rm LS}}(0)$. The estimate of $R_{G_{\rm LS}}(\Delta r)$ was computed by an unbiased sample covariance estimator. The CDF of the correlation distance is presented in Fig. 5(b) for the three Tx positions. The distributions for the positions are similar with the exception for a few large correlation distances for Tx2 and Tx3. The mean value of the correlation distance is 21 m.

In conclusion, we can model the measured path gain $G_{\rm meas}$ as the sum of the distance dependent path gain $G_{\rm d}(d(r))$ in (1), the offset $\bar{G}_{\rm LS}$ that varies from route to route, and the zero-mean fading process $\widetilde{G}_{\rm LS}(r)$. This model is similar in spirit, though different in the details, to the use of random path-loss coefficients and shadowing variances in [17].

C. K-factor

The small-scale fading characteristics was investigated between the two (horizontally omnidirectional) center elements of the arrays. Following the standard modeling assumptions, we describe the fading as Ricean. The K-factor is defined as the ratio between the power of a non-fading component and the power in a Rayleigh fading signal component. Hence, a K-factor equal to zero corresponds to a Rayleigh fading signal envelope, and a large K-factor indicates the non-fading (LOS) component to be dominating. By exploiting the in-phase and quadrature-phase (I/Q) components, the K-factor estimation performance can be significantly improved [18]–[20] compared to methods based on fading envelop statistics only. Common to these I/Q estimators is that they find the amplitude of the non-fading signal component from the largest peak in the Doppler spectrum. In our analysis we use the estimator proposed in [20]

$$\hat{K} = \frac{1}{N}\left[(N-2)\frac{\hat{A}^2}{\hat{\Omega}-\hat{A}^2} - 1\right], \tag{5}$$

where $\hat{A}$ is an amplitude estimate of the non-fading signal component, $\hat{\Omega}$ an estimate of the total signal power, and N is the sample size.

Due to the large wavelength (≈1 m) in our measurements, it was not possible to obtain samples from the spatial domain only and at the same time maintain a reasonable spatial resolution. Instead, $\hat{A}$ was estimated from the largest peak in the joint delay-Doppler spectrum, based on all frequencies and 4 consecutive (spatial) data blocks[1]. The total power estimate, $\hat{\Omega}$, was computed from the squared magnitudes of the frequency transfer function over the 4 blocks.

It can be pointed out that this K-factor estimator, even in situations when the Ricean fading assumption is not fulfilled, has an attractive physical interpretation. For large N, the estimate is the power ratio between the strongest signal in the delay-Doppler spectrum and the received power in all other signal components. There is, however, due to a limited observation windows in frequency and space, no guarantee that $\hat{A}$ is only representing a single physical propagation component. The

[1]An initial coarse estimate was computed by a two-dimensional fast Fourier transform (FFT) of the complex transfer function over the 257 frequency subchannels and over 4 consecutive (spatial) data blocks; using a zero-padding factor of two in each dimension. This initial estimate was then refined iteratively 12 times, where the resolution (in each dimension) was increased by a factor 2 for each iteration.

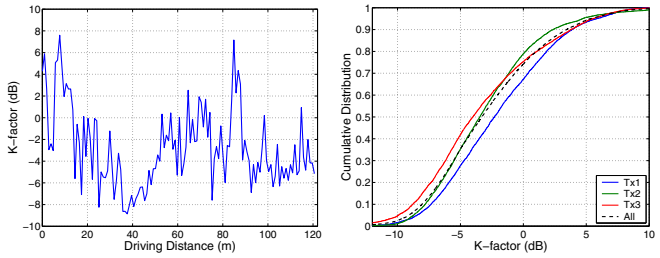

(a) (b)

Fig. 6. (a) Ricean K-factor vs. driving distance along Route 1 for Tx1. (b) CDF for all K-factors measured from each Tx.

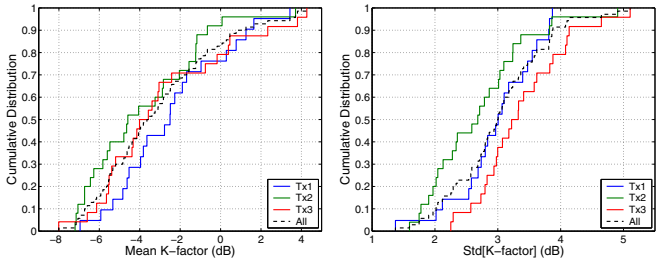

(a) (b)

Fig. 7. CDF of K-factor per-route statistics. (a) Mean. (b) Std.

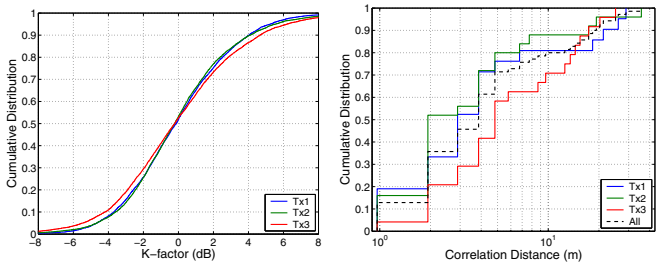

(a) (b)

Fig. 8. (a) CDF for the zero-mean variations $\widetilde{K}_{\mathrm{dB}}$. (b) Correlation distance for the K-factor.

above mentioned interpretation of $\hat{K}$ can be compared with the LOS power factor, K_{LOS}, proposed in [21], which is the ratio between the power in the LOS component, identified from a double-directional channel characterization [22], and the power in all other components. Since the strongest component used in $\hat{K}$, not necessarily corresponds to the LOS component, K_{LOS} and $\hat{K}$ may differ.

Before presenting the statistics for the K-factor in our measurements, we give some examples of characteristics and relations to the measured path gain that have been found to be typical in the scenario. In Fig. 6(a), which shows the K-factor along Route 1 for Tx1, we see that the estimate, in general, shows a quite rapid variation along the route, but also, that it for some rather limited portions of the route is fairly stable. Distinct trends are also found to be maintained over somewhat larger distances along the routes. An example of this is the increase in K between 38–58 m for this route. Comparing this plot with Fig. 3(a), we observe that some of the features in both plots coincides. E.g., the peak in the K-factor at about 85 m corresponds to a local maximum in the path gain, and that the deep dip in the K-factor at 5 m corresponds to a local minimum in the path gain.

The distributions for the K-factor from all routes are shown in Fig. 6(b). The CDFs are, except for a small offset, very similar for the three Tx positions. The mean values (K expressed in dB) are -2.0, -3.0, and -3.3 dB, for Tx1, Tx2, and Tx3, respectively. The standard deviations are 4.3, 4.2, respectively 4.8 dB, for the three Tx positions. Taking all Tx positions together, the total mean and standard deviation is -2.8 and 4.5 dB, respectively. A further examination of the distributions reveals that K in Fig. 6(b) is quite close to log-normally distributed. While lognormal distributions of the K-factor have been described for cellular scenarios [23], they have not yet been described for peer-to-peer scenarios.

To give an overview of the variations in the "local" statistics, the CDFs of the per-route mean and standard deviation are shown in Fig. 7. From these plots it is clear that the per-route mean and standard deviation of the K-factor varies considerably. Considering all Tx locations, the standard deviation for the per-route mean and standard deviation are 3.0 and 0.8 dB, respectively.

Removing the per-route mean, $\bar{K}_{\mathrm{dB}}$, from the K-factor (in dB), in a similar manner as for the large-scale fading in Sec. III-B, we obtain the zero-mean variation $\widetilde{K}_{\mathrm{dB}} = K_{\mathrm{dB}} - \bar{K}_{\mathrm{dB}}$. The CDFs of $\widetilde{K}_{\mathrm{dB}}$ are shown in Fig. 8(a). These distributions are narrower than those for K_{dB} in Fig. 6(b), and have a standard deviation of 3.05, 3.11, and 3.57 dB, for Tx1, Tx2, and Tx3, respectively. However, compared to the large-scale fading, the effect of removing the per-rote mean values for the K-factor is more modest. This might suggest that the K-factor is more dependent on variations in the local environment than the large-scale fading is.

The K-factor in the measured scenario is in general very low. This might be explained by the fact that LOS (or close to LOS) conditions rarely exists due to the low antenna height at both end of the link. Identifying the routes with the largest mean K-factors we find: For Tx1, Route 6 and 7 (which are close to Tx1) have a mean K-factor of 1.3 and 1.6 dB, respectively. Besides these routes, Route 8 has a mean K-factor of 3.4 dB. This route is not exactly close to Tx1 but the street is orientated in a direction towards Tx1. Moreover, a large part of this route has no buildings close to the street as it passes by a cemetery (on both sides of the street). Along this part, there are, however, large trees on both sides of the street. For Tx2, the largest mean K-factor is 3.7 dB for Route 9, which passes very close to Tx2. This route is also oriented in a direction favorable for propagation along the street. No other route mean value is larger than 0 dB for Tx2. Finally, for Tx3, the three largest mean K-factors are 4.3, 3.8, and 2.3 dB for Route 21, 2, and 11, respectively. These three routes are neither close to Tx3, nor in a LOS condition with respect to Tx3. One common property, however, is the orientation of the

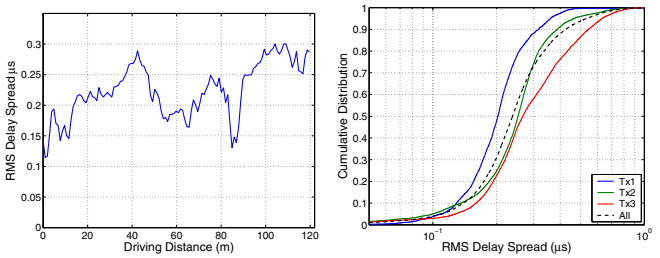

(a) (b)

Fig. 9. RMS delay spread. (a) Delay spread vs. driving distance along Route 1 for Tx1. (b) CDF for all delay spreads measured from each Tx.

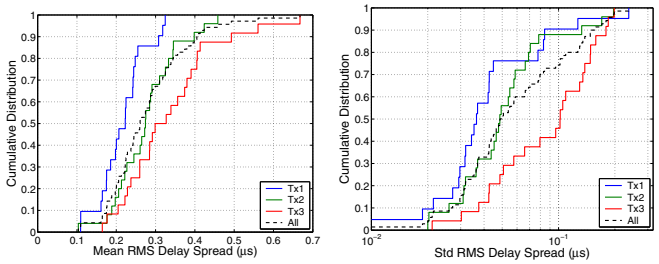

(a) (b)

Fig. 10. RMS delay spread per-route statistics. (a) Mean. (b) Std.

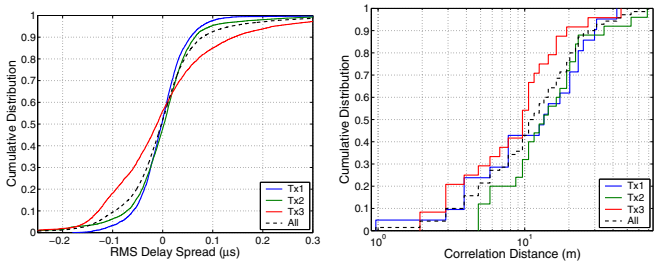

(a) (b)

Fig. 11. (a) CDF for the RMS delay spread zero-mean process $\widetilde{\sigma}_\tau$. (b) CDF for the RMS delay spread correlation distance.

streets, which is in a direction towards Tx3.

The last analyzed property of the K-factor is the correlation distance, which was computed on a per-route basis and in a similar way as for the large-scale fading in Sec. III-B. The result, in Fig. 8(b), shows that the correlation distance for the K-factor, in general, is very small. For all Tx positions together, it is less the 4 m for 50% of the routes, and only exceeds 10 m for 20% of the routes.

D. Delay Spread

The power delay profile (PDP) $\tilde{P}_i(\tau)$ was computed for each measured data block i (separated 0.24 m) by averaging the squared magnitudes of the channel impulse responses over all spatial channels. The impulse responses were obtained by discrete inverse Fourier transformation of the complex frequency transfer functions, which first were multiplied by a Blackman window to reduce the side-lobe levels. The PDPs were then averaged over 4 consecutive data blocks to reduce the variance, giving a profile $P(\tau)$ for about every meter along the measured routes. The RMS delay spread σ_τ, which is defined as the square root of the second central moment of the PDP [24], was computed using a threshold level of 10 dB above the noise. The noise level was estimated from a signal free portion of the PDP by averaging the power spectral density over 2–3 μs.

An example of the estimated RMS delay spread is given in Fig. 9(a), which shows the delay spread vs. driving distance along Route 1 for Tx1. Comparing this with the measured path gain in Fig. 3(a) (as we did for the Ricean K-factor in Fig. 6(a)), we again observe a correlation between the behavior along the route. The peak in the path gain at 85 m, e.g., corresponds to a local minimum in the delay spread. The CDF for σ_τ for all routes is shown in Fig. 9(b). The distribution for Tx3 is slightly different, compared to the other two Tx positions, with a higher proportion of larger delay spreads. Considering all Tx positions, the distribution is close to lognormal. This is in agreement with what has been reported in [25] for a short-range macrocellular environment at 1.9 GHz. The mean values[2] of σ_τ for Tx1, Tx2, and Tx3, are 0.20, 0.24, and 0.28 μs, respectively. From the distributions of the per-route mean ($\bar{\sigma}_\tau$) and standard deviation, presented in Fig. 10, it is clear that there is a large variation between the routes, particularly for $\bar{\sigma}_\tau$. Note that these CDFs are based on a linear σ_τ, but no significant difference was observed for $\bar{\sigma}_\tau$ using the logarithmically weighted mean. The effects of removing the per-route local mean value, by computing the zero-mean process $\widetilde{\sigma}_\tau = \sigma_\tau - \bar{\sigma}_\tau$, is shown by the CDFs in Fig. 11(a). For Tx1 and Tx2, the spread has reduced significantly, while it for Tx3 is still quite large. The standard deviation is 0.07, 0.08, and 0.12 μs, for Tx1, Tx2, and Tx3, respectively.

Finally, the correlation distance for the RMS delay spread is presented in Fig. 11(b). The variation between the routes is very large, ranging from 1 m up to almost 70 m, with a median value of about 10 m.

[2]Computed as $\exp(\mu)$, where μ is the mean of $\log(\sigma_\tau)$.

E. Capacity

The narrowband ergodic MIMO channel capacity for a transmitter without channel state information is given by [4]

$$C = E\Big\{\log_2 \det\Big(\mathbf{I} + \frac{\gamma}{n_{\text{tx}}}\mathbf{H}\mathbf{H}^*\Big)\Big\}, \qquad (6)$$

where $\det(\cdot)$ is the determinant operator, $(\cdot)^*$ the Hermitian transpose, n_{tx} the number of transmit antennas, γ the SNR, and $\mathbf{I}$ is the identity matrix. $\mathbf{H}$ is normalized such that the expected value of its squared Frobenius norm $E\{\|\mathbf{H}\|_F^2\} = n_{\text{rx}}n_{\text{tx}}$, where n_{rx} is the number of receive antennas. In our capacity evaluation, the expectation in (6) was taken over the measured 257 frequency subchannels and over 4 consecutive (spatial) data blocks.

The ergodic MIMO capacity is calculated at a fixed SNR of 10 and 20 dB along the measured routes, using the 7 circularly

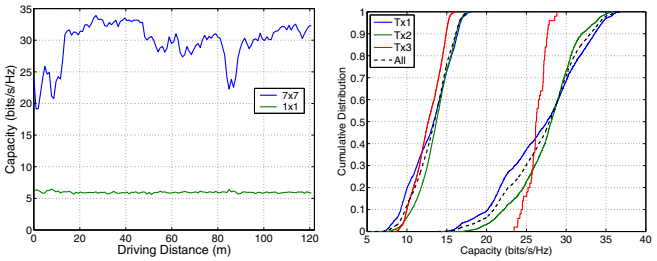

(a) (b)

Fig. 12. (a) Ergodic capacity vs. driving distance along Route 1 for Tx1. (b) CDF for the ergodic capacity measured from each Tx at an SNR of 10 dB (left) and 20 dB (right).

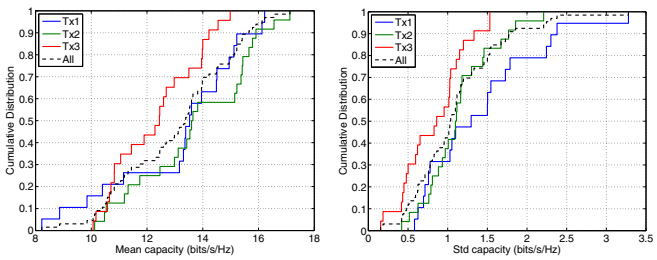

(a) (b)

Fig. 13. Ergodic capacity per-route statistics (SNR: 10 dB). (a) Mean. (b) Std.

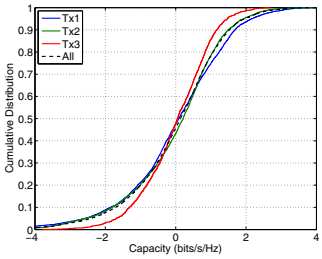

Fig. 14. CDF for the ergodic capacity zero-mean process $\widetilde{C}$ (SNR: 10 dB).

placed elements of the antenna array at both Tx and Rx. The SNR in the channel measurements need to be sufficiently high in order that the calculated capacity not will be affected by the measurement noise. Hence, the capacity analysis is only based on measurements that have an SNR of at least the SNR level the capacity is evaluated for. Considering that the estimated noise level corresponds to a path gain of -138 dB, the measured path gain distribution in Fig. 2(a) reveals that quite a large number of measurements need to be excluded; especially for the 20 dB SNR analysis.

In Fig. 12(a), the blue curve shows the 7×7 MIMO capacity at an SNR of 20 dB along Route 1 for Tx1. As a reference, the calculated SISO capacity between the (horizontally omnidirectional) center elements of the arrays is shown by the green curve. Again, we are going back to the measured path gain in Fig. 3(a) for a comparison. We observe that the capacity variations along the route for the MIMO channel is to a large degree dependent on the path gain; where a higher path gain results in a lower capacity, and vice versa. The capacity distribution for all routes are shown in Fig. 12(b) for an SNR of 10 and 20 dB. The CDF for Tx3 at 20 dB SNR, which only contains a few measurements, is very different compared to the other Tx positions. The capacities could be compared to the ergodic capacity for a 7×7 i.i.d. Rayleigh fading channel matrix, which for an SNR of 10 and 20 dB, are 19.1 and 38.5 bits/s/Hz, respectively. The per-route mean $\bar{C}$ and standard deviation for the ergodic capacity at an SNR of 10 dB are shown in Fig. 13. The variation in $\bar{C}$ is of the same order as for all routes together. The distribution for the zero-mean capacity variations $\widetilde{C} = C - \bar{C}$, at 10 dB SNR for the three Tx positions, is shown in Fig. 14. By removing the per-route mean values, the spread in capacity has been significantly reduced. Hence, the capacity variations in the per-route environment is less than the global variations in the measured scenario.

F. Correlation between channel parameters

The correlation between the different channels parameters is an important property when developing and evaluating channel models. The correlation coefficients for all combinations of the estimated channel parameters and the channel capacity are shown in Table I. The path gain G_{meas} and large-scale fading G_{LS} are expressed in dB scale in the correlation analysis.

The strongest correlations with the capacity are observed for the large-scale fading G_{LS} and the Ricean K-factor K_{dB}. The correlation between capacity and large-scale fading is shown in Fig. 15(a). The figure shows a 2-dimensional histogram where the color indicates the number in each bin. In the figure a major trend can be seen even if the result is scattered. The trend is that for low values of G_{LS} the capacity is high and for large values of G_{LS} the capacity is low. We can see a similar correlation between the K-factor and the capacity in Fig. 15(b). A low K (indicating an amplitude distribution close to Rayleigh) results in high capacity, whereas a large K-factor (indicating a dominant LOS component) gives a low capacity. Furthermore, in Table I, we can see a strong correlation between the K-factor and the large-scale fading; and between the measured path gain G_{meas} and the logarithm of the RMS delay spread.

The correlations are consistent with those observed in cellular macrocells [23], e.g., that higher path gain leads to smaller RMS delay spread.

TABLE I
CORRELATION COEFFICIENTS

	$\log d$	G_{meas}	G_{LS}	K_{dB}	$\log \sigma_\tau$	C
$\log d$	1.00	-0.87	0.09	-0.03	0.50	-0.11
G_{meas}	-0.87	1.00	0.41	0.35	-0.74	-0.24
G_{LS}	0.09	0.41	1.00	0.65	-0.56	-0.69
K_{dB}	-0.03	0.35	0.65	1.00	-0.54	-0.70
$\log \sigma_\tau$	0.50	-0.74	-0.56	-0.54	1.00	0.48
C	-0.11	-0.24	-0.69	-0.70	0.48	1.00

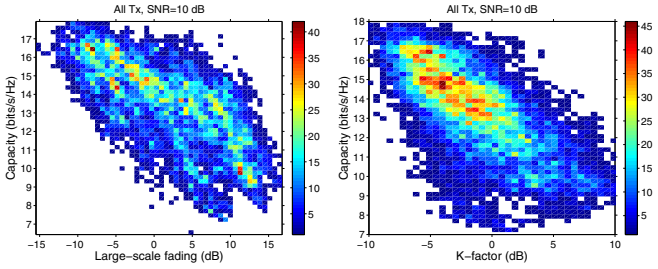

(a) (b)

Fig. 15. Joint distribution. (a) Ergodic capacity and large-scale fading. (b) Ergodic capacity and K-factor.

IV. Conclusions

We have presented results from an urban peer-to-peer MIMO channel measurement campaign at 300 MHz, which is in an important frequency band for tactical communications and emergency services. The MIMO channel was measured along 25 Rx routes, with a total length of about 6 km, for 3 different Tx locations. Basic channel characteristics, which are important for the development and validation of realistic channel models, were extracted from the data, as well as the ergodic capacity for the measured 7×7 MIMO channels at a fixed SNR. A path-loss model was derived for the measured scenario and the distributions of the large-scale fading, the Ricean K-factor, the RMS delay spread, and the ergodic capacity were studied in detail. The correlation distance for the different channel parameters was also examined. The derived path-loss model has a path-loss exponent of 4.15 and the per-route mean delay spread in this scenario varied between 0.1–0.65 μs. The per-route mean K-factors ranged from -8 to 4 dB and the median value of the measured ergodic capacity was about 70% of the capacity for an i.i.d. Rayleigh fading MIMO channel.

For most of the investigated parameters, the statistical analysis shows that the per-route distributions differ considerably compared to the corresponding global distribution for the scenario. Furthermore, we show that many of the investigated parameters are correlated, e.g., the capacity is strongly correlated with the Ricean K-factor and with the large-scale fading, where the two latter parameters also are correlated. Moreover, the delay spread shows a strong correlation with the path loss.

References

[1] R. Vaughan and J. B. Andersen, *Channels, Propagation and Antennas for Mobile Communications*. IEE Electromagnetic Waves Series, 2003.

[2] J. H. Winters, "On the capacity of radio communications systems with diversity in rayleigh fading environments," *IEEE J. Select. Areas Commun.*, vol. 5, pp. 871–878, Jun. 1987.

[3] G. J. Foschini and M. J. Gans, "On limits of wireless communications in a fading environment when using multiple antennas," *Wireless Personal Commun.*, vol. 6, no. 3, pp. 311–335, 1998.

[4] I. E. Telatar, "Capacity of multi-antenna Gaussian channels," *Eur. Trans. Telecommun.*, vol. 10, no. 6, pp. 585–595, Nov./Dec. 1999.

[5] A. F. Molisch and F. Tufvesson, "Multipath propagation models for broadband wireless systems," in *Digital Signal Processing for Wireless Communications Handbook*, M. Ibnkahla, Ed. CRC Press, 2004, ch. 2, pp. 2.1–2.43.

[6] G. D. Durgin, V. Kukshya, and T. S. Rappaport, "Wideband measurements of angle and delay dispersion for outdoor and indoor peer-to-peer radio channels at 1920 MHz," *IEEE Trans. Antennas and Propagat.*, vol. 51, no. 5, pp. 936–944, May 2003.

[7] D. Chizhik, J. Ling, D. Samardzija, and R. A. Valenzuela, "Spatial and polarization characterization of MIMO channels in rural environment," in *Proc. 61st IEEE Veh. Technol. Conf. (VTC '05 Spring)*, vol. 1, Stockholm, Sweden, May 2005, pp. 161–164.

[8] J. Ling, D. Chizhik, D. Samardzija, and R. A. Valenzuela, "Wideband and MIMO measurements in wooded and open areas," in *Proc. IEEE AP-S Int. Symp.*, vol. 3B, Washington, USA, Jul. 2005, pp. 422–425.

[9] "ETSI EN 300 396-2: Trans-European Trunked Radio (TETRA); Technical Requirements for Direct Mode Operation (DMO); Part 2: Radio Aspects," European Telecommunication Standards Institute, Tech. Rep., 2006.

[10] I. Z. Kovács, P. C. F. Eggers, K. Olesen, and L. G. Petersen, "Radio channel description and quality of service for TETRA direct mode operation in forest environments," in *Proc. 54th IEEE Veh. Technol. Conf.*, Atlantic City, USA, Sep. 2001, pp. 1970–1974.

[11] J. R. Hampton, N. M. Merheb, W. L. Lain, D. E. Paunil, R. M. Shuford, and W. T. Kasch, "Urban propagation measurements for ground based communication in the military UHF band," *IEEE Trans. Antennas and Propagat.*, vol. 54, no. 2, pp. 644–654, Feb. 2006.

[12] C. Hendrickson and C. Yerkes, "Wideband wireless peer to peer propagation measurements," in *Thirty-Third Asilomar Conference on Signals, Systems, and Computers*, vol. 1, 1999, pp. 183–189.

[13] J. C. Liberti, J. C. Koshy, T. R. Hoerning, C. C. Martin, J. L. Dixon, A. A. Triolo, R. R. Murray, and T. G. McGiffen, "Experimental results using a MIMO test bed for wideband, high spectral efficiency tactical communications," in *Proc. MILCOM 2005*, Oct. 2005.

[14] G. Eriksson, F. Tufvesson, and A. F. Molisch, "Propagation channel characteristics for peer-to-peer multiple antenna systems at 300 MHz," in *Proc. IEEE GLOBECOM 2006*, San Francisco, USA, Nov. 2006.

[15] R. S. Thomä, D. Hampicke, A. Richter, G. Sommerkorn, and U. Trautwein, "MIMO vector channel sounder measurement for smart antenna system evaluation," *European Transactions on Telecommunications*, vol. 12, no. 5, pp. 427–438, Sep./Oct. 2001.

[16] RUSK channel sounder — Measurement principle. [Online]. Available: http://www.channelsounder.de/ruskchannelsounder.html

[17] V. Erceg, L. J. Greenstein, S. Y. Tjandra, S. R. Parkoff, A. Gupta, B. Kulic, A. A. Julius, and R. Bianchi, "An empirically based path loss model for wireless channels in suburban environments," *IEEE J. Select. Areas Commun.*, vol. 17, no. 7, pp. 1205–1211, Jul. 1999.

[18] C. Tepedelenlioğlu, A. Abdi, and G. B. Giannakis, "The Ricean K factor: Estimation and performance analysis," *IEEE Trans. Wireless. Commun.*, vol. 2, no. 4, pp. 799–810, Jul. 2003.

[19] Y. Chen and N. C. Beaulieu, "Maximum likelihood estimation of the K-factor in Ricean fading channels," *IEEE Communications Letters*, vol. 9, no. 12, pp. 1040–1042, Dec. 2005.

[20] K. E. Baddour and T. J. Willink, "Improved estimation of the Ricean K factor from I/Q samples," in *Proc. 66th IEEE Veh. Technol. Conf. (VTC 2007 Fall)*, Baltimore, MA, USA, Sep./Oct. 2007, pp. 1228–1232.

[21] S. Wyne, A. F. Molisch, P. Almers, G. Eriksson, J. Karedal, and F. Tufvesson, "Outdoor-to-indoor office MIMO measurements and analysis at 5.2 GHz," *IEEE Trans. Veh. Technol.*, vol. 57, no. 3, pp. 1374–1386, May 2008.

[22] M. Steinbauer, A. F. Molisch, and E. Bonek, "The double-directional radio channel," *IEEE Antennas Propag. Mag.*, vol. 43, no. 4, pp. 51–63, 2001.

[23] H. Asplund, A. A. Glazunov, A. F. Molisch, K. I. Pedersen, and M. Steinbauer, "The COST 259 directional channel model–Part II: Macrocells," *IEEE Trans. Wireless. Commun.*, vol. 5, no. 12, pp. 3434–3450, Dec. 2006.

[24] A. F. Molisch, *Wireless Communications*. IEEE Press – Wiley, 2005.

[25] C. Oestges and B. Clerckx, "Modeling outdoor macrocellular clusters based on 1.9-GHz experimental data," *IEEE Trans. Veh. Technol.*, vol. 56, no. 5, pp. 2821–2830, Sep. 2007.